Architected Multimaterial Lattices with Thermally Programmable Mechanical Response

Jochen Mueller, Jennifer A. Lewis,* and Katia Bertoldi*

Architected materials typically maintain their properties throughout their lifetime. However, there is growing interest in the design and fabrication of responsive materials with properties that adapt to their environment. Toward this goal, a versatile framework to realize thermally programmable lattice architectures capable of exhibiting a broader range of mechanical responses is reported. The lattices are composed of two polymeric materials with disparate glass transition temperatures, which are deterministically arranged via 3D printing. By tailoring the local composition and structure, architected lattices with tunable stiffness, Poisson's ratio, and deformation modes controlled through changes in the thermal environment are generated. The platform yields lightweight polymer lattices with programmable composition, architecture, and mechanical response.

1. Introduction

From enhanced relative stiffness, strength, and toughness[1–8] to thermal insulation[9,10] and vibration control,[11,12] lattice structures enable a wide range of properties that are largely defined by their architecture.[13–16] However, these systems maintain these predetermined functions throughout their life time, even when requirements may change. In an attempt to realize responsive structures, shape memory polymers have been introduced to achieve thermally tunable elastic moduli and Poisson's ratios[17–20] as well as adjustable band-gaps.[21] Further, adaptive behavior has been demonstrated in lattices composed of hollow tubes filled with granular particles[22] or magnetorheological fluid suspensions.[23] However, the resulting structures either exhibit long actuation time, lack of reversibility,[17–21] or possess higher structural complexity and cannot be fabricated monolithically.[22,23] Recently, multimaterial 3D printing has emerged as a

powerful platform for fabricating complex structures composed of multiple materials with dissimilar properties.[24–33] If the constituent materials, spacial distribution, and architecture are carefully chosen, multimaterial structures may exhibit effective properties that vary as a function of environmental conditions. For example, a tunable coefficient of thermal expansion has been realized by blending materials with different thermal responses,[34–36] while control over buckling has been achieved in structures comprising materials with different strain rate[37,38] and temperature[33,39,40] sensitivities.

Here, we introduce a new class of thermally tunable lattices that can be monolithically fabricated by multimaterial 3D printing and exhibit programmable responses, including stiffness, Poisson's ratio, and deformation modes (**Figure 1**a,b). To achieve this goal, we combine an active material that substantially weakens upon heating with a passive material with nearly temperature-independent properties over the experimental conditions explored. Guided by numerical analyses, we demonstrate that the distribution of these two materials within the printed lattices give rise to vastly different mechanical properties at elevated temperatures, without altering the behavior under ambient conditions (Figure 1c). While we focused on triangular lattices and used temperature as stimulus, our strategy can be readily extended to other architectures and environmental stimuli, opening new avenues for the design and fabrication of adaptive safety and sports equipment, morphing aerospace structures, and reconfigurable soft robots.

J. Mueller, J. A. Lewis, K. Bertoldi
John A. Paulson School of Engineering and Applied Sciences
Harvard University
Cambridge, MA 02138, USA
E-mail: jalewis@seas.harvard.edu; bertoldi@seas.harvard.edu
J. A. Lewis
Wyss Institute for Biologically Inspired Engineering
Cambridge, MA 02138, USA
K. Bertoldi
Kavli Institute
Harvard University
Cambridge, MA 02138, USA

2. Materials Design Strategy

To realize programmable lattices, we combine a passive material that maintains its properties (including elastic moduli, yield strengths, and failure strength) upon changes in temperature and an active one with properties that vary widely with temperature. Structural integrity is ensured by requiring that these materials exhibit strong adhesion as they are co-printed and cured alongside one another. While not specifically required, we chose two materials with mechanical behavior as close as possible at ambient conditions such that each lattice architecture behaves similarly, independent of how the two materials are spatially arranged on a given lattice.
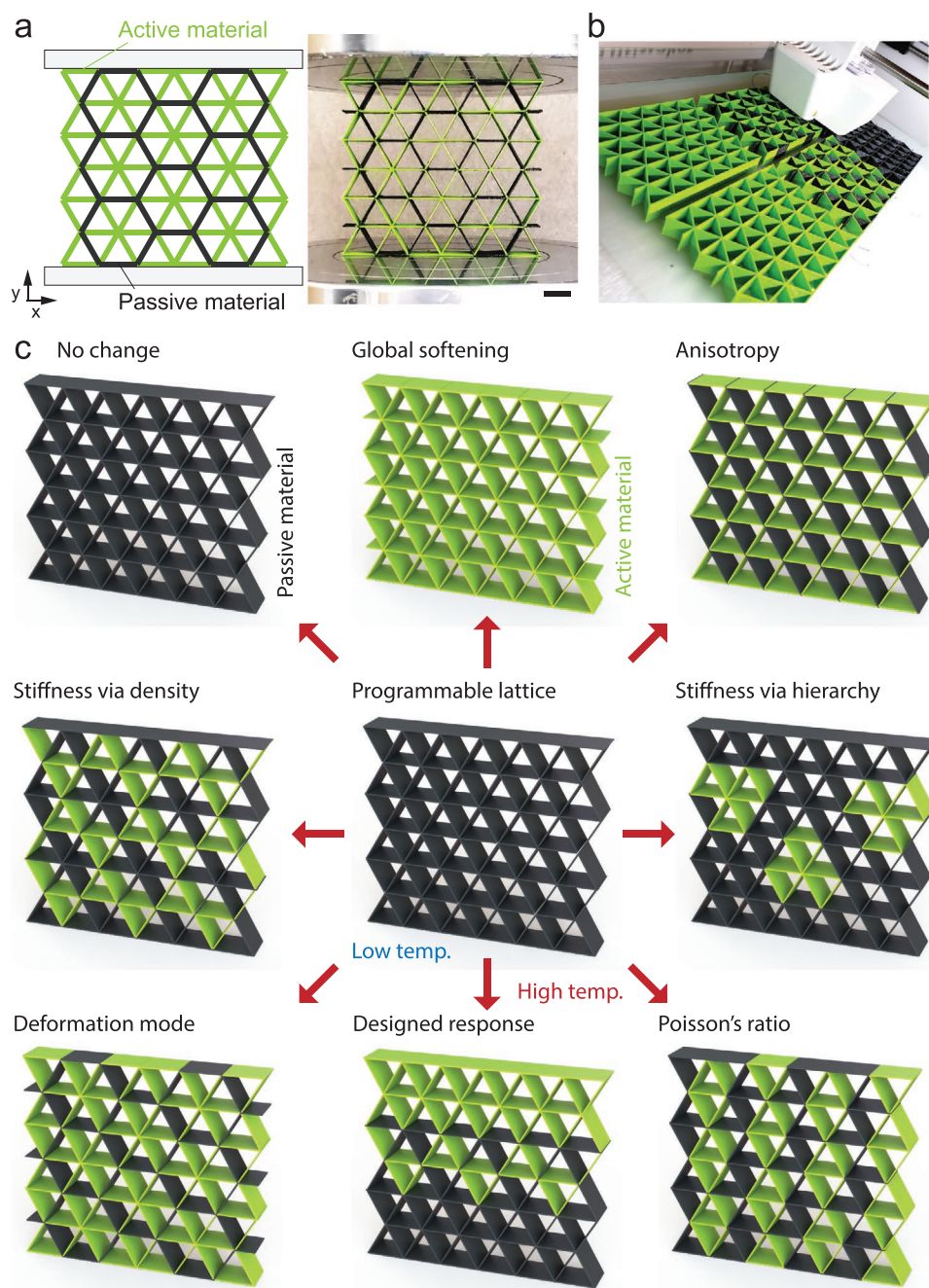
Importantly, we find that these requirements are satisfied by using a modified polyethylene terephthalate (PET) and

**ADVANCED
SCIENCE NEWS**
www.advancedsciencenews.com

**ADVANCED
FUNCTIONAL
MATERIALS**
www.afm-journal.de

Figure 1. Programmable multimaterial lattices. a) Schematic (left) and printed (right) multimaterial triangular lattice constructed by combining an active material (shown in green), which substantially weakens upon heating, with a passive material (shown in black), whose response is temperature independent over the experimental conditions of interest. Scale bar = 10 mm. b) The lattice architectures are monolithically fabricated using fused deposition modeling. c) These lattices can be programmed to exhibit a broad range of mechanical properties and deformation modes at elevated temperature, while exhibiting the same behavior under ambient conditions.

polycarbonate (PC) as the active and passive materials, respectively. To characterize their mechanical response as a function of temperature, we carried out dynamic mechanical analysis (DMA), as shown in **Figure 2**a. Under ambient conditions (i.e., $T = 23$ °C), the two materials exhibit virtually identical storage moduli of $E'_{PET} = 2200$ MPa and $E'_{PC} = 2020$ MPa. However, when the temperature is increased to $T = 100$ °C, E'_{PET} is vastly reduced to 6.7 MPa, while E'_{PC} is only slightly reduced to 1550 MPa,

giving rise to more than two orders of magnitude difference in stiffness. These changes reflect differences between the glass transition temperatures of each material, where $T_{g,PET} = 77$ °C and $T_{g,PC} = 112$ °C.[41] To characterize their response beyond the linear-elastic regime, we carried out uniaxial tensile tests on pure PET and PC dogbone specimens. These data reveal that the elastic moduli of the two materials are quite similar, $E_{PET} = 2112$ MPa and $E_{PC} = 1974$ MPa, at $T = 23$ °C; however, there
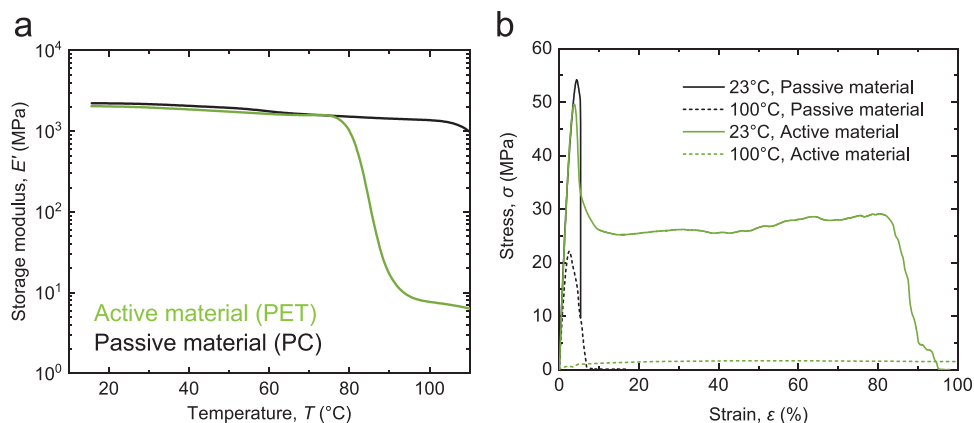
Figure 2. Materials properties. a) Storage modulus versus temperature for the active material (PET - green line) and the passive material (PC - black line) as measured by DMA. b) Uniaxial tension nominal stress-nominal strain curves for PET (green lines) and PC (black lines) at $T = 23\ °C$ (solid lines) and $T = 100\ °C$ (dashed lines).

is a dramatic decrease in E_{PET} to 8.2 MPa, while E_{PC} remains nearly the same at 1506 MPa at $T = 100\ °C$ (Figure 2b). Moreover, PC displays a brittle to plastic behavior at both $T = 23\ °C$ and at $T = 100\ °C$, with a stress that decrease sharply beyond the yield point. By contrast, PET deforms plastically and fails at 90% strain at $T = 23\ °C$ and shows a rubbery behavior with no distinct stress peaks at $T = 100\ °C$.[42]

Next, we created pure PET and PC lattices via fused deposition modeling (FDM). Although our approach can be applied to any lattice geometry, we generated lattices composed of an array of 6 × 6 triangular unit cells (**Figure 3**). All plates in the lattice are made either out of the active or passive material, have in-plane thickness $t = 0.5$ mm, length $l = 12$ mm, aspect ratio $l/t = 24$, and out-of-plane thickness $w = 12$ mm. We then carried out compression tests using a temperature-controlled environmental chamber. The deformation of the active and passive lattices is nearly identical at $T = 23\ °C$ and dominated by two regimes:[4,43,44] a linear elastic region followed by a plateau as expected for stretching dominated lattices (Figure 3b,c). By contrast, when the temperature is increased to $T = 100\ °C$, the response of the passive lattice remains almost unaltered, while both the initial Young's modulus and stress plateau of the active

lattice are substantially reduced. Note that out-of-plane buckling occurred in all samples of the purely active material tested at high temperature due to the significant softening, causing the plateau to temporarily drop upon plastic deformation.

To complement these experiments, we carried out non-linear finite element (FE) simulations, in which we assumed plane-strain conditions, discretized the models with 3-node quadratic beam elements, and used a linearly elastic-perfectly plastic material model with temperature-dependent properties (**Table 1**). We loaded the models imposing a displacement to the top surface (bottom surface remains fixed) and simulated the quasi-static response via the explicit dynamic algorithm. The good agreement between experiment and simulation indicates that FE analyses (Figure 3b,c) can be utilized to rapidly explore the vast design space available for lattices that integrate both active and passive materials.

3. Programmable Multimaterial Lattices

Single-material lattices can either globally soften or maintain the mechanical properties upon an increase in temperature,
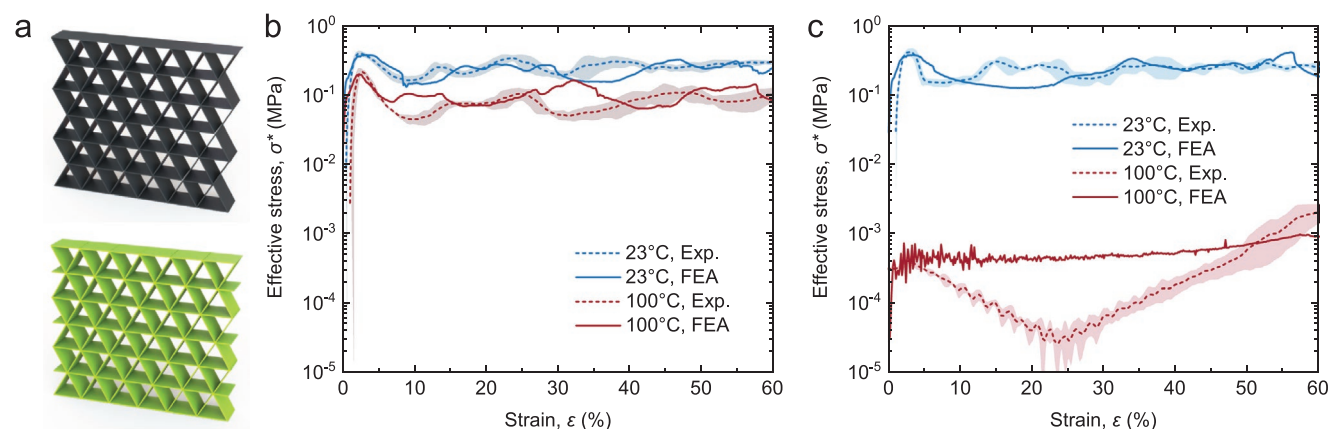
Figure 3. Single-material lattices. a) Schematics of a triangular lattice fabricated from the passive (black) and active (green) materials. b,c) Stress-strain response as measured in experiments (dashed line) and predicted by FE simulations (solid line) at $T = 23\ °C$ (blue lines) and $T = 100\ °C$ (red lines) for triangular lattices made out of the passive (b) and active (c) materials.

**Table 1.** Mechanical properties used in the finite element analysis.

Material	PET	PET	PC	PC
Temperature [°C]	23	100	23	100
Density [g cm^{-3}]	1.38	1.38	1.22	1.22
Poisson's ratio	0.33	0.33	0.33	0.33
Elastic modulus [MPa]	2112	8.2	1974	1506
Yield strength [MPa]	49.6	1.66	54.2	19.2
Yield strain	0.044	2.53	3.8	2.67

as described above. By creating multimaterial lattices with spatially controlled distributions of each material, we can program vastly different mechanical responses at high temperature without altering their behavior under ambient conditions. To achieve this goal, we must ensure good bonding between these materials during FDM. Hence, we produced triangular lattices by first printing PET followed by PC due to its higher T_g.
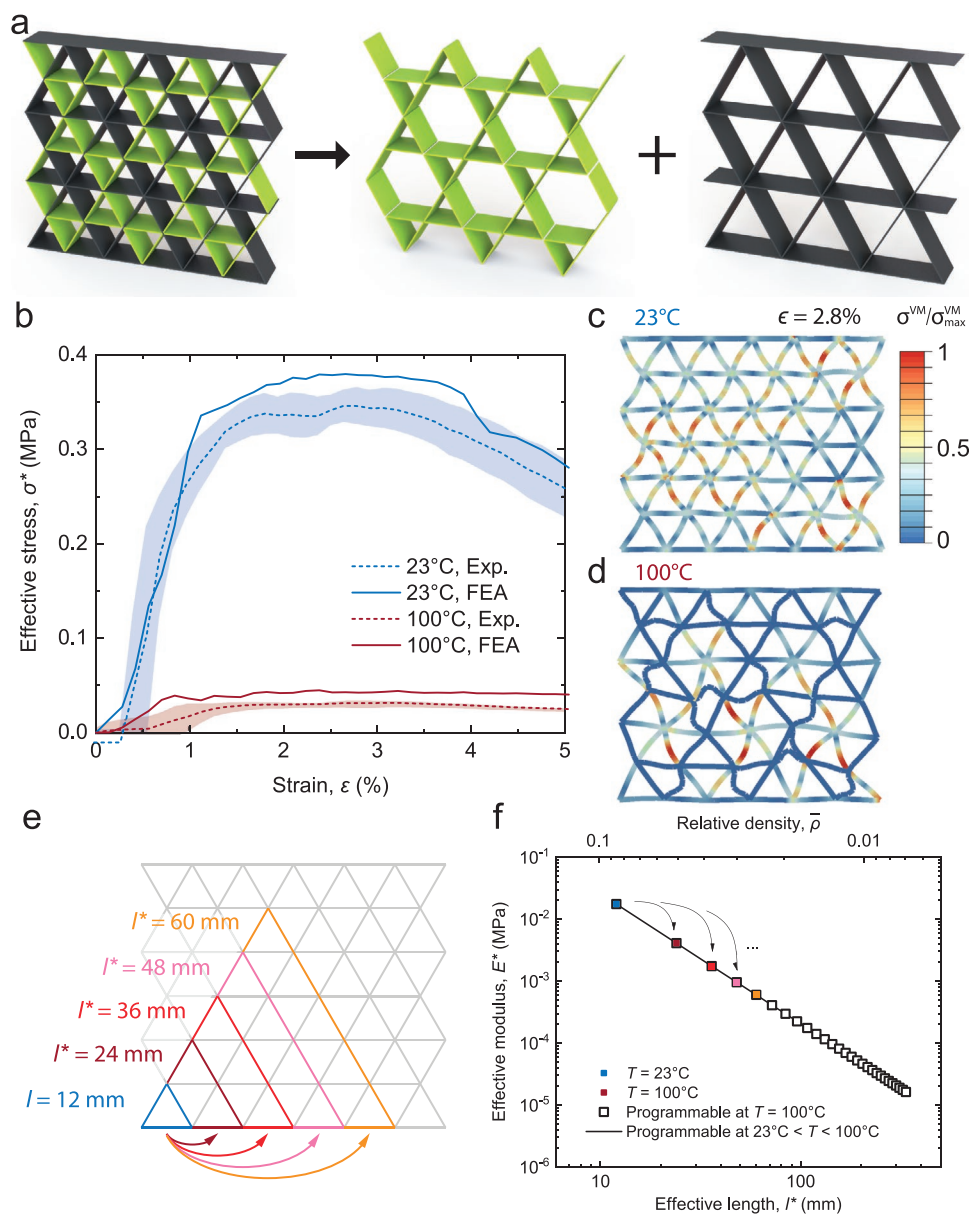
As a first example, we generated multimaterial lattices in which the base structure is programmed to switch from virtually isotropic behavior under ambient conditions to highly anisotropic behavior at high temperature. This is achieved by integrating struts composed of the passive material that are oriented at an angle γ with respect to the loading direction (**Figure 4**). We used FE analyses to investigate the effect of

load directions on the response of these multimaterial lattices during uniaxial compression at both ambient and elevated temperatures and carried out representative experimental measurements for $\gamma = 30°$. At $T = 23°$, we find that the stress–strain response of the multimaterial lattice is almost identical for $\gamma = 0°$, $30°$, and $90°$, indicating an isotropic behavior (Figure 4b,c). However, at high temperature, where we deactivate about two-thirds of the initial structure, the stress plateau for $\gamma = 0°$ is more than an order of magnitude higher than that observed for $\gamma = 30°$, and $90°$. These observations arise due to the alignment of the load with the passive struts, which act as stiff columns despite their global buckling—a behavior we can actively control by distributing the material and by considering intermediate temperature levels. Importantly, the numerical results are confirmed by experiments for $\gamma = 30°$, where the measured stress plateau decreases from $\approx 3 \times 10^{-1}$ MPa at $T = 23$ °C to $\approx 1.1 \times 10^{-3}$ MPa at $T = 100$ °C. The numerically predicted deformation of these lattices for $\gamma = 0°$, $30°$, and $90°$ at $T = 100$ °C are shown in Figure 4d–f.

This paradigm also enables the realization of multimaterial lattices with programmable stiffness and strength by varying their effective relative density as a function of temperature.[13,43,45–47] To demonstrate this, we printed lattices with triangular cells of edge length $l^* = 2l$, which are composed of the passive material while the struts inside these cells are composed of the active material (**Figure 5**a). Since the relative density of a triangular lattice is given by[5,48]
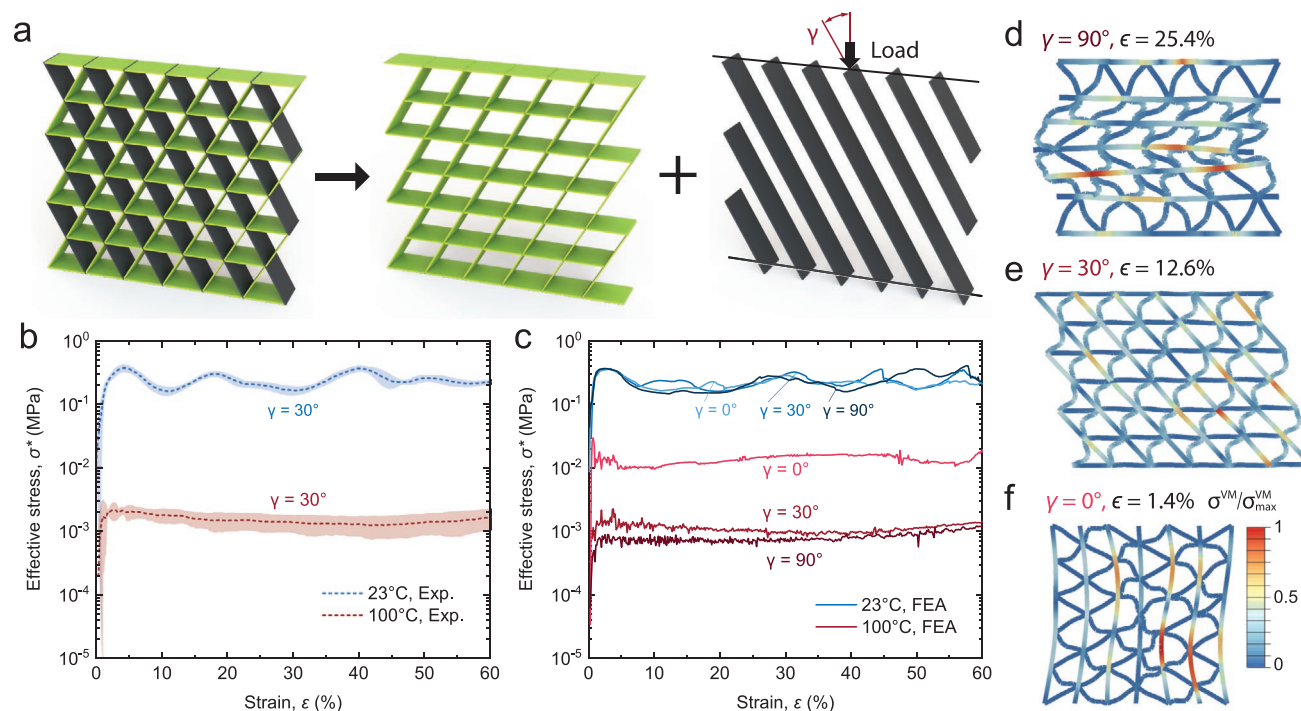
Figure 4. Programmable anisotropy. a) Distribution of the active (green) and passive (black) materials within the lattice. b) Experimentally measured stress-strain curves for $\gamma = 30°$. c) Stress–strain response predicted by FE simulations (solid line) at $T = 23$ °C (blue lines) and $T = 100$ °C (red lines) for $\gamma = 0°$, $30°$, and $90°$. The different shades indicate the load orientation, γ. b) Stress–strain response predicted by FE simulations (solid line) at $T = 23$ °C (blue lines) and $T = 100$ °C (red lines) for $\gamma = 0°$, $30°$, and $90°$. For $\gamma = 30°$ we also report the experimentally measured stress-strain curves (dashed lines). d–f) Numerically predicted deformation at $T = 100$ °C for $(\gamma, \epsilon) = (90°, 25.4\%)$ (d), $(30°, 12.6\%)$ (e), and $(0°, 1.4\%)$ (f). [Note: The color in all snapshots (d-f) corresponds to the normalized von Mises stress.]

**ADVANCED
SCIENCE NEWS**
www.advancedsciencenews.com

**ADVANCED
FUNCTIONAL
MATERIALS**
www.afm-journal.de

Figure 5. Programmable stiffness via density. a) Distribution of the active (green) and passive (black) materials within the lattice. b) Stress–strain response as measured in experiments (dashed line) and predicted by FE simulations (solid line) at $T = 23\ °C$ (blue lines) and $T = 100\ °C$ (red lines). c,d) Numerically predicted deformation at $\varepsilon = 2.8\%$ and $T = 23\ °C$ (c) and $T = 100\ °C$ (d). e) The stiffness of the lattice at high temperature can be programmed by varying the edge length of the triangular cells, l^*, made out of the passive material. f) Evolution of E^* as a function of l^* and $\overline{\rho}$ at $T = 100\ °C$. At room temperature $E^* = 0.01739$ irrespective of l^*. [Note: The color in all numerical snapshots (c,d) corresponds to the normalized von Mises stress.]

$$\overline{\rho} = 2\sqrt{3}(1-\beta)\left(\frac{t}{l^*}\right) \tag{1}$$

where $\beta = 0$ denotes the porosity of the struts, we expect these lattices to have $\overline{\rho} = 0.144$ at $T = 23\ °C$ and $\overline{\rho} = 0.072$ at $T = 100\ °C$ (as $l^* = l$ and $2l$ at $T = 23\ °C$ and $T = 100\ °C$, respectively). Further, since the (effective) modulus in such open-cell lattices, E^*, has been shown to vary as[43]

$$E^* \sim \overline{\rho}^2 \tag{2}$$

we expect $E^* = 42.56$ MPa at $T = 23\ °C$ and $E^* = 10.64$ MPa at $T = 100\ °C$. Importantly, our experiments and FE simulations reveal that $E^* = 41.24$ and 44.52 MPa at $T = 23\ °C$ and $E^* = 4.92$ and 6.28 MPa at $T = 100\ °C$, respectively, confirming the large tunability of their Young's modulus (Figure 5b). The FE simulations also show that, while the stress distribution is relatively homogeneous across both materials at $T = 23\ °C$ (Figure 5c), the stress in the active struts is negligible at $T = 100\ °C$, confirming that an effective change in the relative density has been achieved (Figure 5d). Unlike prior work, in which each temperature corresponds to a specific effective modulus of the

lattice,[17] we can easily program different E^* at a fixed high temperature by varying the edge length of the triangular cells made out of the passive material (Figure 5e). Specifically, if we choose $l^* = nl$ (with n being an integer), we obtain $\bar{\rho} = 0.144$ at low temperature and $\bar{\rho} = 0.144 / n$ at elevated temperature. As a consequence of Equation (2), we then expect $E^* = 42.56$ at $T = 23\ °C$ and $E^* = 42.56/2n$ at $T = 100\ °C$. Simply by varying the number of struts defining the passive triangular cells, we can realize lattices capable of achieving a discrete set of effective Young's moduli at $T = 100\ °C$ while retaining their mechanical properties under ambient conditions (Figure 5f).

We are not limited to discrete values of E^* at elevated temperature, as the Young's modulus can be further programmed by controlling the thickness of the passive triangular cells, thus giving rise to hierarchical architectures. As an exemplar, we show a multimaterial lattice with passive triangular cells with edge length $l^* = 5l$ and thickness $t^* = \sin(\pi/3)l$ (**Figure 6**a). For such architectures, $(1 - \beta) = 0.144$ and Equations (1) and (2) predict that their density and Young's modulus remain the same at $T = 23\ °C$ (i.e., $\bar{\rho} = 0.144$ and $E^* = 42.56$), yet change to $\bar{\rho} = 0.087$ and $E^* = 15.32$ MPa at $T = 100\ °C$. Both experiments and FE simulations confirm the large tunability of the elastic modulus with measured values of $E^* = 39.30$ and 44.52 MPa at $T = 23\ °C$ and $E^* = 3.73$ and 4.78 MPa at $T = 100\ °C$, respectively (Figure 6b). Moreover, numerical snapshots indicate that the failure behavior of these hierarchical architectures vary with temperature (Figure 6c,d). Under ambient conditions, these

architected multimaterial lattices fail layer by layer (Figure 6c). By contrast at $T = 100\ °C$, the active material experiences little stress and the structure fails at the narrowest cross-section of the triangular unit cells composed of the passive material (Figure 6d).

Our approach can also be harnessed to realize architected multimaterial lattices with target stress–strain response at elevated temperature. As an example, we can design a lattice that exhibits an initial linear behavior at $T = 100\ °C$ followed by three distinct plateau regions by printing only passive material in the bottom struts, only active material in the top struts, and a combination of both materials in the central region (**Figure 7**a). At $T = 100\ °C$, the top (active) region is the first to deform plastically, introducing a plateau at $\approx 3 \times 10^{-4}$ MPa (Figure 7b)—a value comparable to that displayed by the purely active lattice (Figure 3). The central region starts to buckle and plastically deform once the top section is fully compacted, which leads to a second plateau at $\approx 4 \times 10^{-2}$ MPa. Finally, at $\varepsilon \approx 0.5$, the central region is fully solidified and the deformation is transmitted to the bottom region, which enters the plastic regime via local buckling, leading to the formation of a third plateau at $\approx 1 \times 10^{-1}$ MPa.

Next, we created architected multimaterial lattices with distinct deformation behavior at ambient and elevated temperatures. We first generate lattices whose deformation at ambient temperature is dominated by stretching and by bending at higher temperatures. While stretching dominated structures
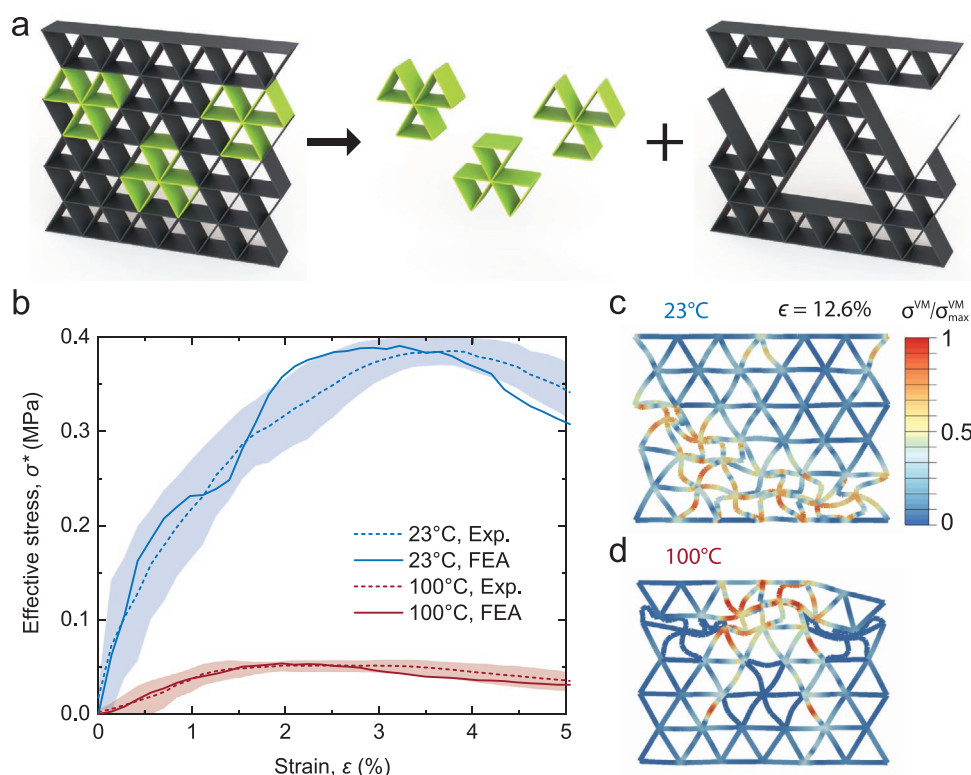
Figure 6. Programmable stiffness via hierarchy. a) Distribution of the active (green) and passive (black) materials within architected lattices. b) Stress–strain response as measured in experiments (dashed line) and predicted by FE simulations (solid line) at $T = 23\ °C$ (blue lines) and $T = 100\ °C$ (red lines). c,d) Numerically predicted deformation at $\varepsilon = 12.6\%$ and $T = 23\ °C$ (c) and $T = 100\ °C$ (d). [Note: The color in all numerical snapshots (c,d) corresponds to the normalized von Mises stress.]
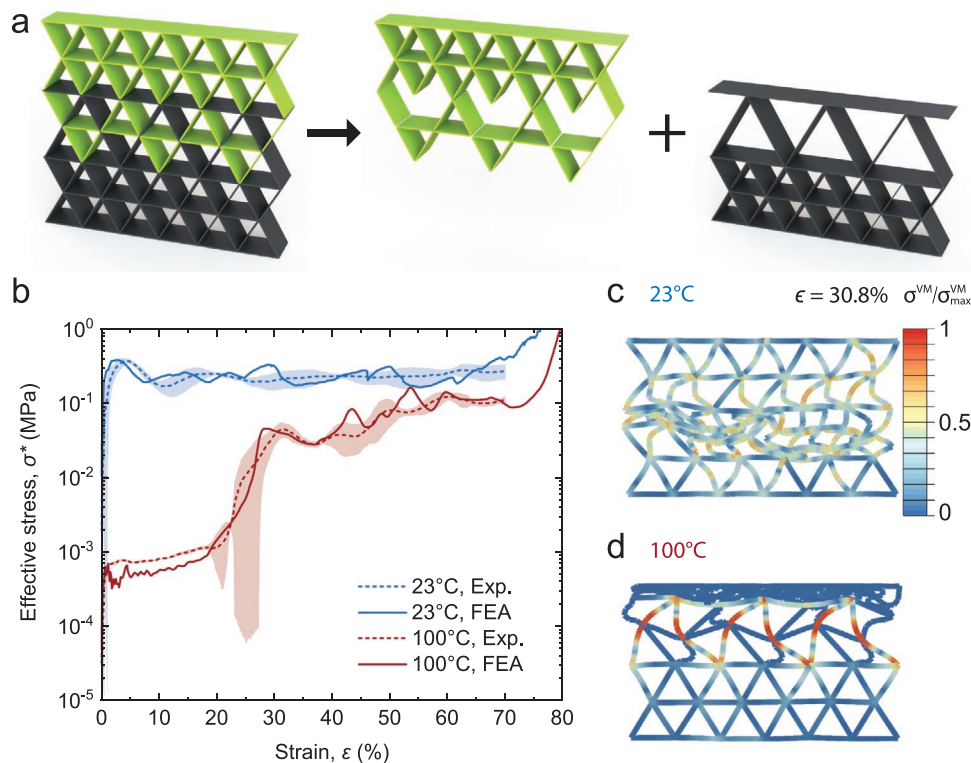
Figure 7. Programmable stress-strain behavior. a) Distribution of the active (green) and passive (black) materials within the lattice. b) Stress–strain response as measured in experiments (dashed line) and predicted by FE simulations (solid line) at $T = 23$ °C (blue lines) and $T = 100$ °C (red lines). c,d) Numerically predicted deformation at $\varepsilon = 30.8\%$ and $T = 23$ °C (c) and $T = 100$ °C (d). [Note: The color in all numerical snapshots (c,d) corresponds to the normalized von Mises stress.]

are characterized by high stiffness and strength, bending-dominated ones are typically used in energy-absorbing applications due to their low transmitted (peak) stress and high toughness.[13,43] This change in deformation mode depends upon the connectivity number, Z, the average number of connections at joints.[43] For $Z \geq 6$, 2D lattice structures are stretching dominated, whereas for $Z \leq 3$, they are considered bending-dominated.[43] Remarkably, this programmable transition in mechanical behavior can be achieved by arranging the passive material to form a hexagonal unit cell, while all remaining struts are composed of the active material (**Figure 8**a). At $T = 23$ °C, all struts have similar mechanical properties, $Z = 6$, and the stress-strain curve displays a high initial peak stress followed by several bumps indicative of a layer by layer failure (Figure 8b,c). Such behavior is typical of stretching-dominated lattices and known to be advantageous for structural applications that require high stiffness and strength.[43] By contrast, at $T = 100$ °C, the connectivity reduces to $Z = 3$ due to the deactivation of the active struts, mechanically revealing the hexagonal lattice structure (Figure 8b,d). The resulting stress-strain behavior lacks any distinct peaks and the stress plateaus remain relatively constant until densification at $\varepsilon > 60\%$—a behavior typical of bending-dominated structures.[4]

As a final demonstration, we show that tunable Poisson's ratio can be achieved by realizing a re-entrant multimaterial lattice architecture that typically possesses negative Poisson's ratio[49,50] (**Figure 9**a). At ambient temperature, this lattice effectively behaves as a triangular lattice and displays a positive Poisson's ratio, $\nu = 0.063$ (Figure 9b,c). However, as the temperature is increased, the active material eventually softens and exposes the re-entrant lattice (Figures 9d). At $T = 100$ °C, the Poisson's ratio sharply decreases to $\nu = -0.48$. Note that the Poisson's ratios reported in Figure 9b are extracted from FE simulations at $\varepsilon = 0.01$ and averaged over four nodes in the central part of the structure (Figure 9b, inset).[51]

4. Summary and Conclusion

In summary, we have shown that architected multimaterial lattices that combine thermally active and passive materials can be programmed to support a broad range of temperature-dependent mechanical responses. We have demonstrated this by integrating materials with similar mechanical properties under ambient conditions that differ substantially at high temperature. Hence, by programming the spatial distribution of these two materials within the lattice, we can encode myriad mechanical responses at elevated temperatures. Specifically, we have programmably defined their elastic modulus and Poisson's ratio, switched from isotropic to anisotropic behavior, and altered their deformation modes from a bending- to stretching-dominated response. Looking ahead, our approach can be extended to arbitrary 2D and 3D architectures as well as new polymeric materials that respond to different stimuli to program a broader range of stimuli-responsive mechanical properties. By augmenting our approach with stochastic optimization
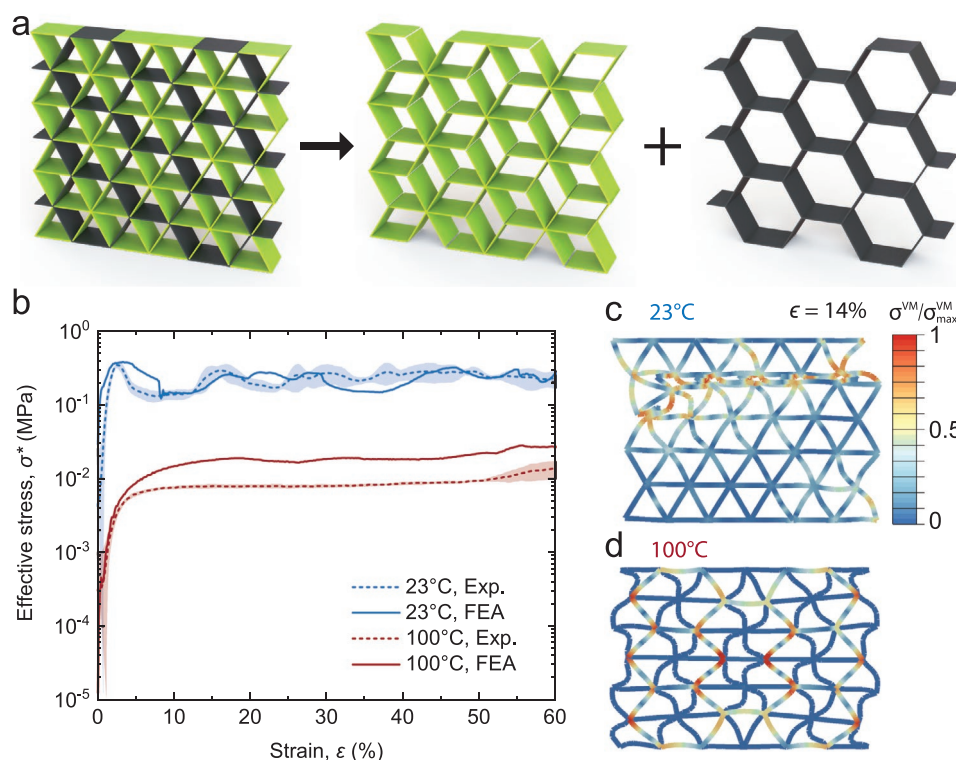
Figure 8. Programmable deformation modes. a) Distribution of the active (green) and passive (black) materials within the lattice. b) Stress–strain response as measured in experiments (dashed line) and predicted by FE simulations (solid line) at $T = 23$ °C (blue lines) and $T = 100$ °C (red lines). c,d) Numerically predicted deformation at $\varepsilon = 14\%$ and $T = 23$ °C (c) and $T = 100$ °C (d). [Note: The color in all numerical snapshots (c,d) corresponds to the normalized von Mises stress.]

algorithms to solve the inverse design problem, we can rapidly identify target designs for a given set of applications, including light-weight, adaptive, and robotic structures.

5. Experimental Section

3D Printing: Single- and multimaterial lattices were printed using fused deposition modeling with a nozzle diameter of 0.4 mm (Ultimaker, S5 Utrecht, Netherlands). The height of the first layer was set at 0.1 mm, while the height of all subsequent layers was set at 0.3 mm with an infill density of 100%. The print speed was 50 mm s^{-1} with a retraction distance of 3 mm for both materials. To print the modified polyethylene terephthalate (PET - Taulman3D, Indianapolis, USA), the nozzle temperature was set to 250 °C, the heated glass substrate was held at 45 °C, the flow was set to 105%, and the fan speed was set to 40%. To print the polycarbonate (Ultimaker, Utrecht, the Netherlands), the nozzle temperature was set to 270 °C, the heated glass substrate was held at 110 °C, and the fan speed was set to 0%. When co-printing these materials, the PC was printed after the PET due to its higher glass-transition temperature to ensure bonding. In this case, the heated glass substrate was set to 80 °C.

Dynamic Mechanical Analysis (DMA): DMA tests were conducted on a DMA Q800 (TA Instruments, Inc., New Castle, DE 19720, USA) using 3D printed samples with size 20 mm × 12 mm × 1.5 mm (note that each sample was measured using a digital caliper). A dual cantilever setup (which is the general purpose mode for evaluating thermoplastics and highly damped materials) was used, clamped the samples at both ends, and flexed them at the center. The storage modulus was measured from $T = 10$ °C to $T = 160$ °C at 2 °C min^{-1}. In all our tests, the DMA

furnace was cooled to $T = 10$ °C using liquid nitrogen. Then, the samples were mounted and their ends were clamped using a torque meter set to 9 *in.lbs*. After closing the furnace, the authors waited 2 min for the sample to adjust its temperature to $T = 10$ °C, re-opened the hood, and re-adjusted the screws to the given torque, before closing the furnace again. The DMA was set to the multi-frequency strain mode and run at a frequency of 1 Hz and 0.1% strain.

Tension and Compression Tests: Tension and compression tests under displacement control were conducted using an Instron 5566 testing machine (Instron, Norwood, MA, USA) equipped with either a 10 N or 1000 N load cells. The testing speed was set to 10 mm min^{-1}. High temperature properties were tested using an Instron 3119 environmental chamber (Instron, Norwood, MA, USA). The temperature accuracy was verified with an external thermocouple located near the sample and showed good agreement with the temperature set by the environmental chamber.

Finite Element Analysis: The commercial FE software Abaqus 2019 (3D Systems, Rock Hill, SC, USA) was used to numerically investigate the response of the lattices. The Abaqus/Explicit solver was employed for all the simulations. Plane strain conditions were assumed and 3-node quadratic beam (B22) was used with an element size of 2 mm. The mesh size was ascertained through a mesh refinement study. The materials were modeled assuming linearly elastic-perfectly plastic properties using the materials properties reported in Table 1. The models were placed between two rigid plates, held in place only by friction (a frictional coefficient of 0.3 was used). They were loaded by moving the top rigid plate vertically until a maximum nominal strain of 70% was reached at a strain rate of 1 s^{-1}, while keeping the bottom rigid plate fixed. In all the analyses, linear and quadratic bulk viscosity factors of 0.06 and 1.2 were used, respectively, with a minimum step size of 1×10^{-7} s.
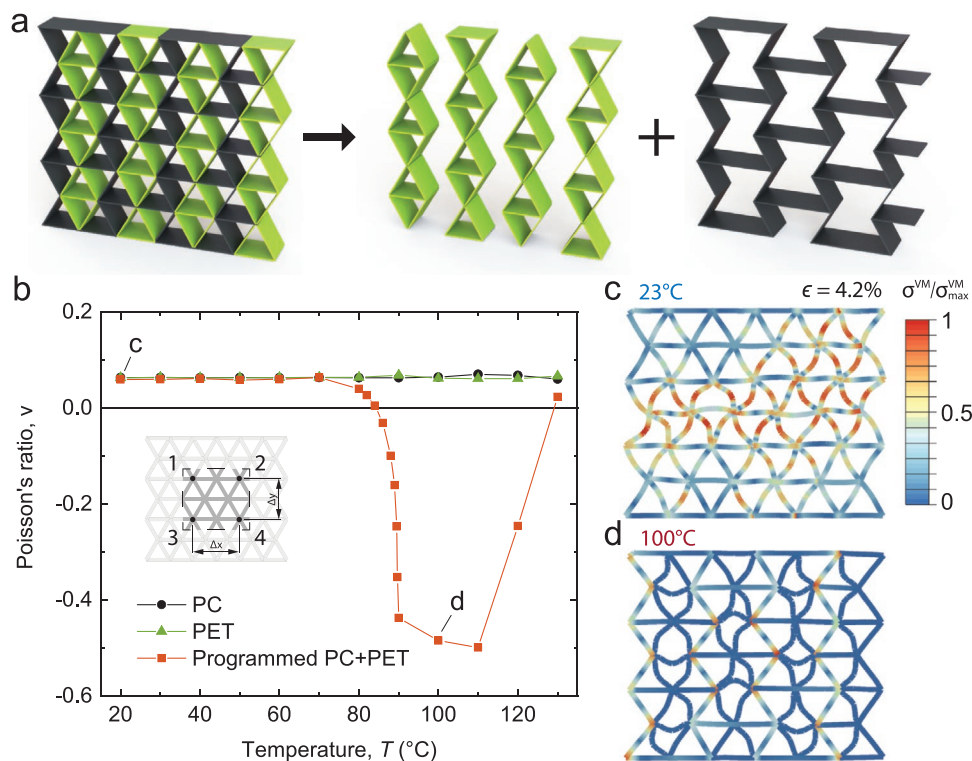
Figure 9. Programmable Poisson's ratio. a) Distribution of the active (green) and passive (black) materials within the lattice. b) Numerically predicted evolution of the effective Poisson's ratio as a function of temperature for single-material lattices made out of PC (black markers), PET (green markers), and the programmed lattices shown in (a) (red markers). c,d) Numerically predicted deformation at $\varepsilon = 4.2\%$ and $T = 23\,°C$ (c) and $T = 100\,°C$ (d). [Note: The color in all numerical snapshots (c,d) corresponds to the normalized von Mises stress.]

Conflict of Interest

The authors declare no conflict of interest.

Data Availability Statement

The data that support the findings of this study are available from the corresponding author upon reasonable request.

[1] X. Zheng, H. Lee, T. H. Weisgraber, M. Shusteff, J. DeOtte, E. B. Duoss, J. D. Kuntz, M. M. Biener, Q. Ge, J. A. Jackson, S. O. Kucheyev, N. X. Fang, C. M. Spadaccini, *Science* **2014**, *344*, 1373.

[2] T. A. Schaedler, A. J. Jacobsen, A. Torrents, A. E. Sorensen, J. Lian, J. R. Greer, L. Valdevit, W. B. Carter, *Science* **2011**, *334*, 962.

[3] L. R. Meza, A. J. Zelhofer, N. Clarke, A. J. Mateos, D. M. Kochmann, J. R. Greer, *Proc. Natl. Acad. Sci. USA* **2015**, *112*, 11502.

[4] J. Mueller, K. H. Matlack, K. Shea, C. Daraio, *Adv. Theory Simul.* **2019**, *2*, 1900081.

[5] J. T. Muth, P. G. Dixon, L. Woish, L. J. Gibson, J. A. Lewis, *Proc. Natl. Acad. Sci. USA* **2017**, *114*, 1832.

[6] J. R. Raney, B. G. Compton, J. Mueller, T. J. Ober, K. Shea, J. A. Lewis, *Proc. Natl. Acad. Sci. USA* **2018**, *115*, 1198.

[7] J. Mueller, J. R. Raney, D. M. Kochmann, K. Shea, *Adv. Sci.* **2018**, *5*, 1800728.

[8] J. Mueller, J. R. Raney, K. Shea, J. A. Lewis, *Adv. Mater.* **2018**, *30*, 1705001.

[9] M. F. Ashby, *Philos. Trans. R. Soc., A* **2006**, *364*, 15.

[10] M. S. Al-Homoud, *Build. Environ.* **2005**, *40*, 353.

[11] E. Baravelli, M. Ruzzene, *J. Sound Vib.* **2013**, *332*, 6562.

[12] Y. Chen, T. Li, F. Scarpa, L. Wang, *Phys. Rev. Appl.* **2017**, *7*, 024012.

[13] M. F. Ashby, T. Evans, N. A. Fleck, J. Hutchinson, H. Wadley, L. Gibson, *Metal Foams: A Design Guide*, Elsevier, Boston, MA **2000**.

[14] D. Mahmoud, M. A. Elbestawi, *J. Manuf. Mater. Process.* **2017**, *1*, 13.

[15] L. J. Gibson, *MRS Bull.* **2003**, *28*, 270.

[16] L. Jin, R. Khajehtourian, J. Mueller, A. Rafsanjani, V. Tournat, K. Bertoldi, D. M. Kochmann, *Proc. Natl. Acad. Sci. USA* **2020**, *117*, 2319.

[17] C. Yang, M. Boorugu, A. Dopp, J. Ren, R. Martin, D. Han, W. Choi, H. Lee, *Mater. Horiz.* **2019**, *6*, 1244.

ADVANCED
SCIENCE NEWS
www.advancedsciencenews.com

ADVANCED
FUNCTIONAL
MATERIALS
www.afm-journal.de

[18] J. Rossiter, K. Takashima, F. Scarpa, P. Walters, T. Mukai, *Smart Mater. Struct.* **2014**, *23*, 045007.

[19] D. Restrepo, N. D. Mankame, P. D. Zavattieri, *Int. J. Solids Struct.* **2016**, *100*, 485.

[20] M. A. Wagner, T. S. Lumpe, T. Chen, K. Shea, *Extreme Mech. Lett.* **2019**, *29*, 100461.

[21] C. Nimmagadda, K. H. Matlack, *J. Sound Vib.* **2019**, *439*, 29.

[22] Y. Wang, B. Ramirez, K. Carpenter, C. Naify, D. C. Hofmann, C. Daraio, *Extreme Mech. Lett.* **2019**, *33*, 100557.

[23] J. A. Jackson, M. C. Messner, N. A. Dudukovic, W. L. Smith, L. Bekker, B. Moran, A. M. Golobic, A. J. Pascall, E. B. Duoss, K. J. Loh, et al., *Sci. Adv.* **2018**, *4*, eaau6419.

[24] R. L. Truby, J. A. Lewis, *Nature* **2016**, *540*, 371.

[25] M. A. Skylar-Scott, J. Mueller, C. W. Visser, J. A. Lewis, *Nature* **2019**, *575*, 330.

[26] C. Bader, D. Kolb, J. C. Weaver, S. Sharma, A. Hosny, J. Costa, N. Oxman, *Sci. Adv.* **2018**, *4*, eaas8652.

[27] J. O. Hardin, T. J. Ober, A. D. Valentine, J. A. Lewis, *Adv. Mater.* **2015**, *27*, 3279.

[28] D. Kokkinis, M. Schaffner, A. R. Studart, *Nat. Commun.* **2015**, *6*, 1.

[29] X. Li, J. M. Zhang, X. Yi, Z. Huang, P. Lv, H. Duan, *Adv. Sci.* **2019**, *6*, 1800730.

[30] A. D. Valentine, T. A. Busbee, J. W. Boley, J. R. Raney, A. Chortos, A. Kotikian, J. D. Berrigan, M. F. Durstock, J. A. Lewis, *Adv. Mater.* **2017**, *29*, 1703817.

[31] M. Wehner, R. L. Truby, D. J. Fitzgerald, B. Mosadegh, G. M. Whitesides, J. A. Lewis, R. J. Wood, *Nature* **2016**, *536*, 451.

[32] D. B. Kolesky, K. A. Homan, M. A. Skylar-Scott, J. A. Lewis, *Proc. Natl. Acad. Sci.* **2016**, *113*, 3179.

[33] Y. Zhang, M. Velay-Lizancos, D. Restrepo, N. D. Mankame, P. D. Zavattieri, *Matter* **2021**, *4*, 1990.

[34] J. Qu, M. Kadic, A. Naber, M. Wegener, *Sci. Rep.* **2017**, *7*, 40643.

[35] J. Liu, T. Gu, S. Shan, S. H. Kang, J. C. Weaver, K. Bertoldi, *Adv. Mater.* **2016**, *28*, 6619.

[36] J. W. Boley, W. M. van Rees, C. Lissandrello, M. N. Horenstein, R. L. Truby, A. Kotikian, J. A. Lewis, L. Mahadevan, *Proc. Natl. Acad. Sci. USA* **2019**, *116*, 20856.

[37] S. Janbaz, K. Narooei, T. van Manen, A. Zadpoor, *Sci. Adv.* **2020**, *6*, 25eaba0616.

[38] A. Bossart, D. M. Dykstra, J. van der Laan, C. Coulais, arXiv preprint, arXiv:2006.05149, **2020**.

[39] Z. Zhao, C. Yuan, M. Lei, L. Yang, Q. Zhang, H. Chen, H. J. Qi, D. Fang, *Phys. Rev. Appl.* **2019**, *11*, 044074.

[40] C. Yuan, X. Mu, C. K. Dunn, J. Haidar, T. Wang, H. Jerry Qi, *Adv. Funct. Mater.* **2018**, *28*, 1705727.

[41] J. Brandrup, E. H. Immergut, E. A. Grulke, A. Abe, D. R. Bloch, *Polymer Handbook*, vol. 89, Wiley, New York **1999**.

[42] P. A. Thrower, *Materials in Today's World*, McGraw-Hill College, New York **1992**.

[43] V. Deshpande, M. Ashby, N. Fleck, *Acta Mater.* **2001**, *49*, 1035.

[44] Y. Liu, X.-C. Zhang, *Int. J. Impact Eng.* **2009**, *36*, 98.

[45] L. J. Gibson, M. F. Ashby, *Cellular Solids: Structure and Properties*, Cambridge University Press, Cambridge, UK **1999**.

[46] S. D. Papka, S. Kyriakides, *J. Mech. Phys. Solids* **1994**, *42*, 1499.

[47] L. Gong, S. Kyriakides, W.-Y. Jang, *Int. J. Solids Struct.* **2005**, *42*, 1355.

[48] N. A. Fleck, V. S. Deshpande, M. F. Ashby, *Proc. Royal Soc. A: Math., Phys. Eng. Sci.* **2010**, *466*, 2495.

[49] L. J. Gibson, M. F. Ashby, G. Schajer, C. Robertson, *Proc. Royal Soc. London. A. Math. Phys. Sci.* **1982**, *382*, 25.

[50] F. Robert, *J. Elasticity* **1985**, *15*, 427.

[51] K. Bertoldi, P. M. Reis, S. Willshaw, T. Mullin, *Adv. Mater.* **2010**, *22*, 361.

2105128 (10 of 10)